Combustion and Flame 157 (2010) 1783–1794

Contents lists available at ScienceDirect

Combustion and Flame

journal homepage: www.elsevier.com/locate/combustflame

Plasma assisted cavity flame ignition in supersonic flows

Hyungrok Do *, Mark A. Cappelli, M. Godfrey Mungal

Mechanical Engineering Department, Stanford University, United States

ARTICLE INFO

Article history:
Received 10 November 2009
Received in revised form 26 January 2010
Accepted 19 March 2010
Available online 3 April 2010

Keywords:
Nonequilibrium plasma
Supersonic
Plasma-assisted combustion
Pulsed plasma
Scramjet
Cavity
Expansion tube
Flame stabilization

ABSTRACT

A nanosecond pulsed plasma discharge located within a wall cavity is used to ignite jet flames (hydrogen and ethylene) in supersonic crossflows. The nonequilibrium plasma is produced by repetitive pulses of 15 kV peak voltage, 20 ns pulse width and 50 kHz repetition rate. Sonic fuel jets are injected into free stream air of Mach numbers Ma = 1.7 to Ma = 3.0. The flow pattern and shockwaves induced by the fuel jets and cavity are characterized by Schlieren imaging and planar laser induced fluorescence is used to image the distribution of OH radicals. Combustion is found to be enhanced by the plasma discharge, with the time evolution of the flame suggesting that enhancement is caused by the reduction in ignition delay time. Similar trends are observed with both hydrogen and ethylene fuel injection. The experimental results for hydrogen combustion are interpreted using a simple model in which the pulsed plasma serves as a repetitive source of reactive radicals. The reaction kinetics following radical production is evolved numerically, confirming a reduction in ignition delay comparable to that seen in the experiments. The model description allows us to predict how a broader range of plasma operation conditions will affect combustion.

© 2010 The Combustion Institute. Published by Elsevier Inc. All rights reserved.

1. Introduction

The problem of igniting and sustaining combustion in high speed gas flows continues to be a critical issue in aerospace propulsion. The advent of supersonic/hypersonic aircraft has prompted the demand for stable combustion in supersonic flows and reliable thrust over a broad range of flight conditions. Traditional methods for igniting and sustaining combustion in supersonic gas flows include geometric surface alterations, such as the addition of cavities [1–3], ramp injectors [4,5], wall steps [6] and angled combustor walls [7]. These methods generate recirculation regions for fuel and oxidizer to mix and reside long enough to be ignited and burned. In addition to promoting mixing, these geometric alterations reduce the local flow speed and elevate the local static temperature. Of these options, cavity wall stabilization seems to be one of the most common of the methods studied as it is relatively simple to implement and results in strong performance sensitivity to variation in the cavity length-to-depth ratio. An overview of cavity flame stabilization is provided by Ben-Yakar and Hanson [1]. The reader is referred to Kim et al. [8], Lin et al. [9] and Fang et al. [10] for studies of the flow field induced by cavities and the flow properties conducive to flame stabilization.

A less common, but increasingly relevant supersonic combustion stabilization method includes the use of plasma discharges. Nonequilibrium plasma discharges are able to enhance combustion because of their capacity to efficiently produce reactive radical species. There have been several studies that demonstrate how plasmas benefit flame stability in subsonic environments [11–15]. However, there have been fewer studies of plasma-enhanced supersonic combustion, and most of these focus on the ignition of diffusion flames in supersonic flows in conjunction with geometric alterations. In such a hybrid scheme, the plasma facilitates chemical reactions and the geometric alteration provides a favorable flow condition for flame holding. For example, in recent studies, an arc jet was injected into the downstream region of a fuel injection ramp [7], and a quasi-direct-current (DC) discharge plasma was generated within a surface cavity [6]. One study included the use of a microwave plasma discharges without the use of cavities or ramps, to enhance ignition of supersonic premixed combustible gases [16].

Our goal is to develop an effective flame stabilization method for supersonic combustion that employs a highly nonequilibrium pulsed plasma. In the study described here, a nanosecond repetitively pulsed discharge is used in tandem with a wall cavity. The cavity is critical to flame stabilization by providing a region of flow recirculation. In the absence of recirculation of the flow, the residence time of the supersonic flow (τ_{res}) may be shorter than the ignition delay time (τ_{ign}) of the fuel/air mixture. Under such conditions, little or no combustion will take place. The application of the

* Corresponding author at: Bldg. 520, Room 520I, Stanford, CA 94305-3032, United States. Fax: +1 650 723 1748.
E-mail address: hyungrok@stanford.edu (H. Do).

0010-2180/$ - see front matter © 2010 The Combustion Institute. Published by Elsevier Inc. All rights reserved.
doi:10.1016/j.combustflame.2010.03.009

Table 1
Pressures of the three sections corresponding to flow conditions.

	Run condition	1	2	3	4	5	6	7	8	9
Initial pressures	Driver section (psia)	45	67	177	196	206	225	274	404	615
	Buffer section (psig)			75	75	75	85	110	165	235
	Driven section (torr)	23	10	17	19	15	19	19	22	26
	Expansion section (torr)	56	25	29	7	27	21	21	18	20
Freestream conditions	Mach number	1.7 ± 0.03	2.0 ± 0.03	2.4 ± 0.05	2.4 ± 0.05	2.3 ± 0.05	2.5 ± 0.05	2.6 ± 0.05	2.9 ± 0.08	3.0 ± 0.08
	Simulated flight Mach number	5.0–5.5	6.0–7.5	7.5–3.0	7.5–3.5	7.0–9.0	7.5–9.0	8.0–9.0	8.5–9.0	9.0–10.0
	Stagnation enthalpy (MJ/kg)	1.0 ± 0.05	2.0 ± 0.05	2.4 ± 0.08	2.4 ± 0.08	2.6 ± 0.1	2.6 ± 0.1	2.9 ± 0.15	3.3 ± 0.15	3.3 ± 0.15
	Static temperature (K)	900 ± 30	1250 + 50	1240 ± 50	1300 ± 50	1480 + 50	1300 ± 50	1330 ± 50	1360 ± 50	1520 ± 70
	Static pressure (kPa)	25 ± 1	16 ± 1	18 ± 1	24 ± 1	25 ± 1	17 ± 1	23 ± 1	23 ± 2	24 + 2
	Test time (μs)	700 ± 50	500 + 50	350 ± 50	350 ± 50	300 + 50	300 ± 50	300 ± 50	300 ± 50	200 ± 50
	Flow velocity (m/s)	1000 ± 20	1380 ± 25	1650 ± 30	1690 ± 30	1940 ± 40	1820 ± 40	2060 ± 40	2370 ± 65	2380 ± 65
	Freestream flow path length during the test time (m)	0.7	0.7	0.6	0.6	0.6	0.5	0.6	0.7	O.6
	Freestream Re_x upstream of jet injection nozzle: $X = 0.05$ m($\times 10^5$)	1.24	0.64	0.87	1.10	1.06	0.64	1.24	1.37	1.45
	Establishment length for laminar boundary layer upstream of jet injection nozzle: 3X (m) (Davies and Bernstein, 1969)	0.15	0.15	0.15	0.15	0.15	0.15	0.15	0.15	0.15
	Effective test time: test time – establishment length/flow velocity (μs)	550	390	260	260	220	220	230	240	150
	Boundary layer thickness upstream of jet injection nozzle (mm)	0.71	0.99	0.85	0.76	0.77	0.86	0.71	0.68	0.66
Re_D of hydrogen jet: jet to freestream momentum ratio (J) = 4 jet nozzle diameter (D) = 2 mm ($\times 10^5$)		1.39	1.23	1.99	2.65	2.54	2.04	2.98	3.71	4.14

nonequilibrium plasma serves to reduce τ_{ign} while the addition of the cavity serves to increase τ_{res}. Consequently, when combined, these two modifications are expected to greatly enhance flame stability.

2. Experimental setup

Our experimental facility includes an expansion tube used to generate conditions comparable to those of the supersonic flow in the combustor of a scramjet engine. Details of the expansion tube are provided in Ref. [17] and only a brief description is given here. The expansion tube is a circular stainless steel tube (alloy 304) of 14 cm inner diameter (16.5 cm outer diameter) connected to a cylindrical dump tank (60 cm diameter and 122 cm length). The tube has three parts divided by two diaphragms: the driver (2 m length), driven (7.3 m length) and expansion (2.8 m length) sections. A test section (welded stainless steel cube, 30 cm × 30 cm × 30 cm inside, 1.27 cm wall thickness) for observations and measurements is located between the expansion section and the dump tank. Each flow condition corresponds to a pressure ratio of the three sections as shown in Table 1.

A jet in crossflow model is installed in the test section. The model, simulating the wall of a supersonic combustor in a scramjet engine, is a rectangular aluminum plate (5.5 × 4 in., 1 in. thickness) containing a jet injection nozzle, electrodes and a ceramic plate embedded for electrical insulation of the pulsed discharge electrodes. A heat-treated 22° angle sharp leading edge (A2 tool steel) is attached on the front side of the model flush with the upper surface. The overview of Ben-Yakar and Hanson [1] suggested that a cavity of 7–10 L/D ratio, where L is the cavity length and D is the depth, can serve as an adequate flame-holder for a range of flow conditions. A ratio of $L/D = 7$ with $L = 21$ mm and $D = 3$ mm, is chosen following these guidelines. A schematic of the cavity model is presented in Fig. 1. Our studies described here focus on conditions in which the electrodes are placed within the cavity. As shown in the figure, the front step of the cavity is perpendicular to the oncoming flow while the back step is inclined at 25° to the horizontal plane. The cavity shaped groove extends spanwise across the entire width of the aluminum model, however, a portion of the cavity is fabricated into a 2 × 4 cm ceramic (Cotronics, 960 machinable alumina (dielectric strength: 200 V/mil)) insert which serves to isolate the discharge electrodes. The ceramic insert has two holes (1 mm diameter) to accommodate the discharge electrodes (1 mm diameter, 2% thoriated tungsten rods) separated by 3 mm, and aligned in the streamwise direction. The thoriated tungsten has a relatively low work function (2.6 eV) in comparison to other possible electrode materials. The upstream electrode is used as the cathode and is positioned 8 mm downstream of the front step of the cavity. The oblique jet injection nozzle (1 mm diameter), angled 30° from the horizontal plane (pointing toward the

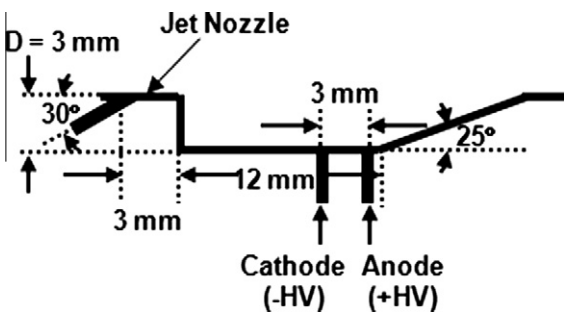

Fig. 1. The schematic of the cavity model.

downstream direction), is located 3 mm upstream of the front step of the cavity. The nozzle and two electrodes are on the streamwise directed center line of the aluminum model.

A nonequilibrium plasma is produced by high voltage pulses (typically 15 kV peak voltage, 10 ns pulse width and 50 kHz repetition rate) applied between the two electrodes. The cathode is negatively biased (−7.5 kV) while the anode is positively biased (+7.5 kV) at the peaks of the pulses. The voltage pulses are formed by a pulse generator (FID Technology, Model F1112) powered by two DC power supplies and triggered by a high speed switching circuit. A high voltage DC power supply (Sorensen, Model DCS600-1.7E) provides the main power consumed by the plasma and the plasma generation system. A supplemental DC power supply (HP, Model 6264B) is used for providing power to a refrigeration system for cooling the pulse generator.

Hydroxyl (OH) planar laser induced fluorescence (PLIF) is used to visualize the ground state OH radical distribution. The characterization of the ground state OH distribution provides a qualitative indicator of the presence of combustion and the physical location of the flame region. A Nd:YAG laser (Continuum Precision, Model PL8000) that pumps a dye laser (Lumonics, Model HD-500) equipped with a frequency doubling unit (Lumonics, Model HyperTRAK-1000) for generating 3–7 mJ per pulse at 283 nm (10 Hz repetition rate), is used to excite the A-X(1,0) Q1(7) electronic transition of the OH molecule. The laser beam is transformed into a thin sheet by a set of cylindrical concave and spherical convex lenses. The sheet of the laser beam is projected vertically, through a quartz window on the upper face of the test section, on the center line of the model's surface, in a plane coincident with the electrodes and jet injection nozzle. The spectrally filtered (using a narrow band pass filter from 305 to 325 nm) laser induced fluorescence is captured by an intensified camera (Andor, iStar ICCD) at right angles to the plane of the laser sheet. The limiting resolution of these images is approximately 80 μm, estimated from the camera array size of 512×512 pixels imaged onto a 40×40 mm region of the flow. The images depict noncalibrated OH excited state and ground state concentration fields, which serve to provide a qualitative depiction of the flame structure. Schlieren imaging [18] is carried out with an ultra fast framing camera (Imacon 486 intensified CCD camera) and a pulsed xenon flash lamp (Hamamatsu, Model E6611).

3. Results and discussion

3.1. Cavity flame stabilization

Conventional cavity flame stabilization, not aided by the plasma discharge, is first recorded under various flow conditions. Fig. 2a shows a set of time sequential Schlieren images illustrating the structure of the flow field with hydrogen jet injection and a cavity located downstream of the jet in the presence of a supersonic air freestream flow of total enthalpy, $h_0 \sim 2.0$ MJ/kg (condition 2 in Table 1). The freestream flow direction is from left to right in all of the figures presented here. Before the beginning of the test time (0 μs in Fig. 2a), the fully developed sonic jet first starts to bend towards the downstream direction because of the helium gas flow that precedes the test gas flow. At the beginning of the test time (when the test gas arrives), three shockwaves (Fig. 2b), induced by (i) the jet injection, (ii) the front step and (iii) the inclined back wall of the cavity, appear in the images. It is noteworthy that fluctuations in the angle of the first shockwave, induced by the jet injection, suggest some unsteadiness in the freestream flow. This unsteadiness is distinctly unrelated to disturbances caused by the complex flows in the vicinity of the cavity. Also, we observe that the jet trajectory of the fuel is bent over the shear layer of the cavity, promoting fuel entrainment across the shear layer into the cavity. As rarefaction waves and the helium gas flow from the driver section arrives at the test section, the test time ends (at approximately 500 μs) and the shockwaves vanish.

Fig. 3 depicts OH PLIF images taken with different freestream flow conditions and jet momentum ratio, J_n, which is defined as the ratio of the normal component of the jet momentum flux to the free stream momentum flux (here the factor of 1/2 comes from the 30° injection relative to the free stream flow direction):

$$J_n = \frac{(\rho u^2)_{jet}}{2(\rho u^2)_{\infty}}$$

where ρ is the density and u is the velocity of the jet and freestream flows, respectively.

In Fig. 3a, we have $J_n \sim 3$, with $h_0 \sim 3.3$ MJ/kg (condition 8) for the freestream air flow, (b) $J_n \sim 4.5$ with $h_0 \sim 2.9$ MJ/kg (condition 7) for the air flow, and (c) $J_n \sim 5.5$ with $h_0 \sim 2.6$ MJ/kg (condition 6) for the air flow. The images are taken 200 μs after the beginning of the test time (the test time is approximately 300 μs at this flow condition). The ground state OH distributions shown in the images depict flame regions that are auto-ignited both inside and outside of the cavity. A filamentary flame is observed in the windward side of the jet (Fig. 3a and b) above the cavity while a stronger and broader flame is sustained inside the cavity (Fig. 3a–c). The two flames are separated by the trajectory of the fuel jet core where the fuel concentration is too high to be ignited. In studies conducted by Heltsley et al. [17,19], filamentary flames are also observed in the windward side of jets in relatively high enthalpy flow conditions ($h_0 > 2.75$ MJ/kg) on a flat wall in the absence of a cavity with $J_n \sim 4$ and normal injection configurations. Coincidentally, the filamentary flames are not observed at lower enthalpy conditions (Fig. 3c: $h_0 \sim 2.6$ MJ/kg) in the current study because ignition of the filamentary flames depends on the strength of the upstream shockwave induced by the jet injection, and the shock strength increases as the flow enthalpy increases. These flames are seen to reside just behind the shockwave and are presumed to be ignited by the resulting temperature and pressure elevation. It is noteworthy that, no flame is observed on the leeward side in the previous flat wall study of Heltsley et al. [19] because the flow residence time (τ_{res}) is too short to sustain a flame in that region in the absence of a cavity. Lower enthalpy cases are also investigated in the present study (as low as 1.0 MJ/kg, condition 1). No detectable OH is observed in the cavity when the stagnation enthalpy of the freestream flow is lower than 2.0 MJ/kg (conditions 1 and 2).

Fig. 4 shows a set of time sequential OH PLIF images, each separated by 40 μs, depicting the time evolution of an auto-ignited flame in a cavity. The freestream flow condition is $h_0 \sim 2.9$ MJ/kg (run condition 7). The time $t = 0$ μs is used for reference, corresponding to the beginning of the test time. The first ignition event is observed to appear on the back wall of the cavity at 80 μs. This suggests that the cavity flame ignition delay time is approximately 80 μs. The ignition delay time referred to here (τ_{ign}) includes the mixing time and the time attributed to the kinetics of combustion reactions. The cavity flame is ignited due to the high enthalpy of the freestream flow. The high enthalpy appears to be sufficient to initiate combustion under this flow condition (the static temperature in the cavity and the boundary layer approaches the stagnation temperature of the freestream flow which typically exceeds 2000 K). This condition is referred to as auto-ignition. All of the freestream flows tested in this study are either of high enthalpy or high static temperature and are expected to ignite these flammable fuel gas mixtures after some finite time duration (τ_{ign}). The lowest static temperature condition generated in this study (run condition 1) is 900 K, which exceeds the auto-ignition temperature of hydrogen, known to be approximately 850 K [20]. However, a cavity flame is not observed in this

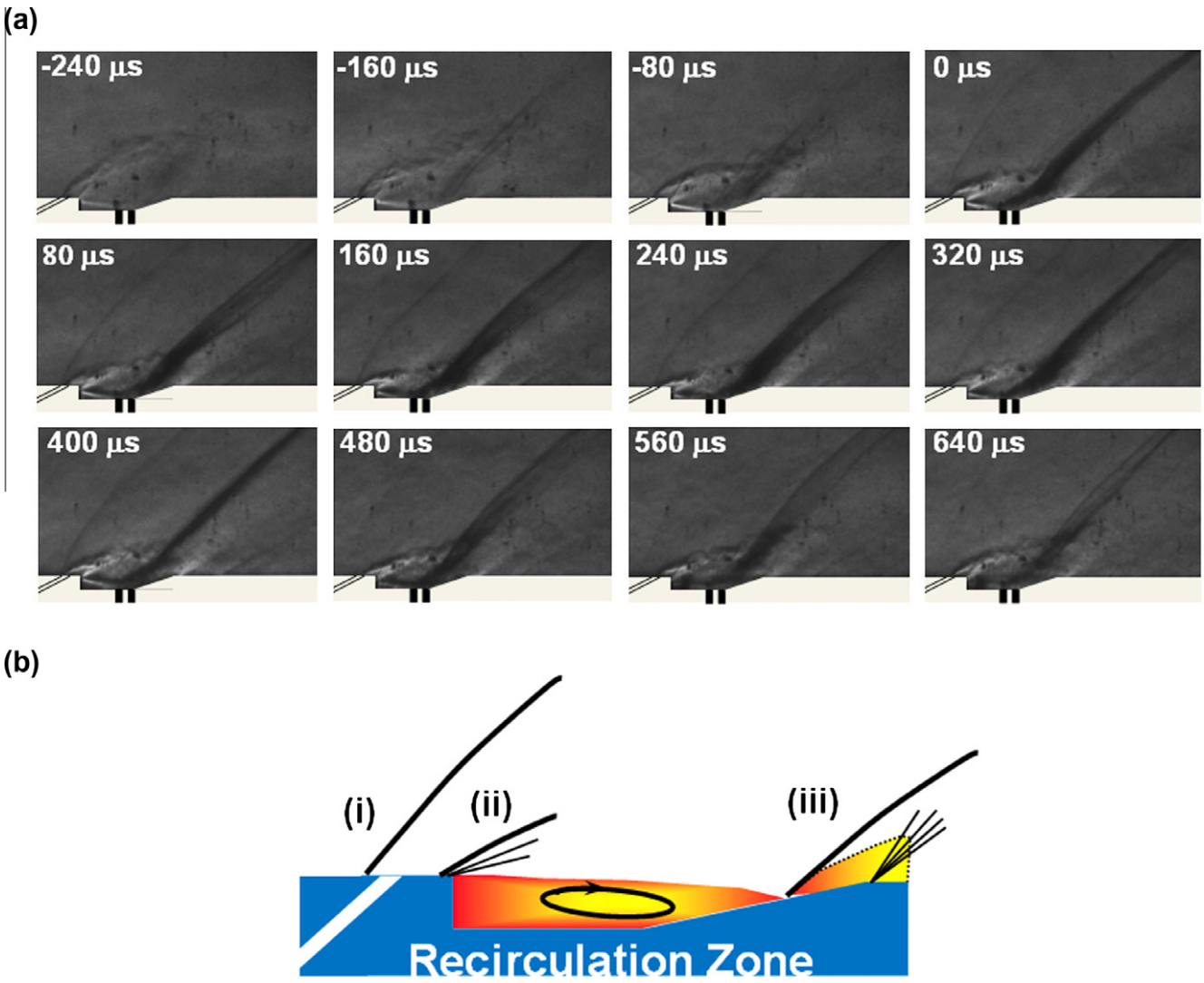

Fig. 2. (a) A set of time sequential Schlieren images illustrating the flow field in the presence of a supersonic freestream flow (run condition 2): the test time starts at 0 μs and ends at approximately 500 μs, and (b) a schematic of three shock waves induced by (i) the jet injection, (ii) the front step and (iii) the inclined back wall of the cavity.

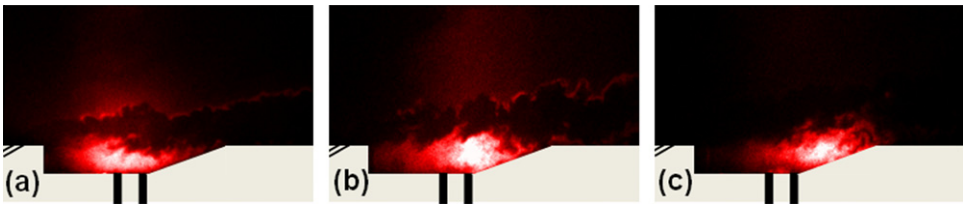

Fig. 3. Three OH PLIF images showing auto-ignited hydrogen cavity flames in the absence of a plasma in supersonic flows of three different enthalpies: (a) run condition 8 ($J_n \sim 3$), (b) run condition 7 ($J_n \sim 4.5$) and (c) run condition 6 ($J_n \sim 5.5$).

low static temperature case. We attribute this to the short residence time. A flame can not be sustained if the flow residence time (τ_{res}) in the cavity is shorter than τ_{ign}. In addition, a close inspection of Fig. 4 reveals that the cavity flame initiates near the back wall (at about 80 μs) and propagates both towards the front of the cavity and towards the freestream flow. One general observation is that the flame does not appear to penetrate deep into the freestream flow.

3.2. Application of a pulsed plasma discharge in a cavity

The pulsed plasma discharge is applied within the cavity to further enhance flame stability. Fig. 5 provides a comparison of auto-ignited cavity flames and plasma assisted cavity flames at two different flow conditions. The images in the presence of the plasma (Fig. 5b and d) are taken 1 μs after a discharge pulse and approximately 200 μs after the start of the test time. The plasma is turned on well before the beginning of the test time. Fig. 5a and b corresponds to the case of $J_n \sim 4$ hydrogen injection and $h_0 \sim 3.3$ MJ/kg (condition 8) air flow, while Fig. 5c and d corresponds to $J_n \sim 3.5$ hydrogen injection and $h_0 \sim 2.9$ MJ/kg (condition 7) air flow. All of the images are taken 200 μs after the beginning of the test time (approximately 300 μs test time at this flow condition). Fig. 5a and c are taken without the plasma, and Fig. 5b and d are in the presence of the plasma. Cavity flames in Fig. 5a and

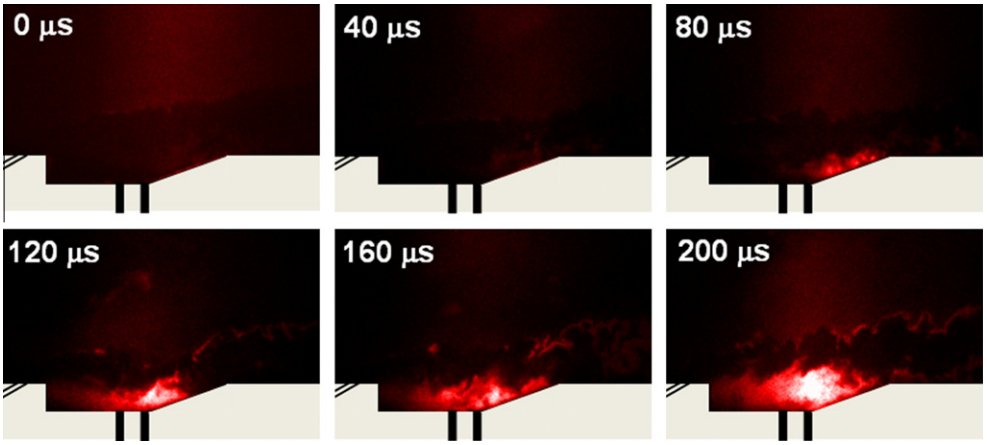

Fig. 4. Time sequential OH PLIF images in the absence of a plasma separated by 40 μs with a supersonic crossflow (run condition 7) and a hydrogen jet ($J_n \sim 4.5$).

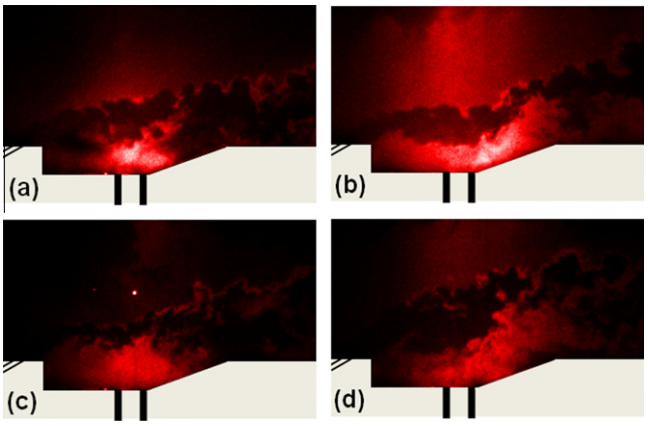

Fig. 5. OH PLIF images of a cavity flame in supersonic flows of two different enthalpies: (a) without the plasma and (b) in the presence of the plasma in run condition 8 flow (hydrogen jet, $J_n \sim 4$), and (c) without the plasma and (d) in the presence of the plasma in run condition 7 flow (hydrogen jet, $J_n \sim 3.5$).

c are typical of auto-ignited flames, residing primarily within the cavity, and with limited flame propagation into the freestream flow. The plasma enhanced cavity flames seen in Fig. 5b and d clearly appear to extend into the freestream flow on the leeward side of the fuel jet. In the presence of the plasma, the propagation of the cavity flames are limited by the trajectories of the fuel jet cores. The fuel jet trajectory is an intrinsic limitation for flame propagation, setting a boundary for the flammable regions in the flow.

The trailing flames that extend into the freestream flow provide compelling evidence that flame holding is possible in these high speed flow regimes. As mentioned above, the flame tail resides on the leeward side of the fuel jet where the flow speed is much higher than the flow speed inside the cavity. A flame cannot survive the high speed flow in the absence of a cavity, as shown in the previous study conducted by Heltsley et al. [17,19]. This is despite the fact that the fuel is relatively well mixed with the freestream flow in that region. The fuel mixing (in the leeward side) of a jet in supersonic crossflow has been studied both experimentally [21] and numerically [22]. The flame tail can survive the high speed flow because the cavity flame and the pulsed plasma in the cavity serve as a source of heat and radicals, both capable of shortening the ignition delay time (τ_{ign}) of the well mixed flammable mixture. The combustion mechanism can overcome the slowest initiation reaction producing radicals from a fuel/oxidizer mixture to make τ_{ign} shorter, if sufficient radicals are supplied to initiate branching/propagation reactions.

Time sequential OH PLIF images presented in Fig. 6 depict the effect of the plasma on the cavity flame, through a reduction of ignition delay time (τ_{ign}) of the hydrogen jet flame inside the cavity. The images are taken in the presence of the pulsed plasma at the same freestream flow condition as in Fig. 4 (condition 7). A comparison of Figs. 4 and 6 reveals two differences. The flame

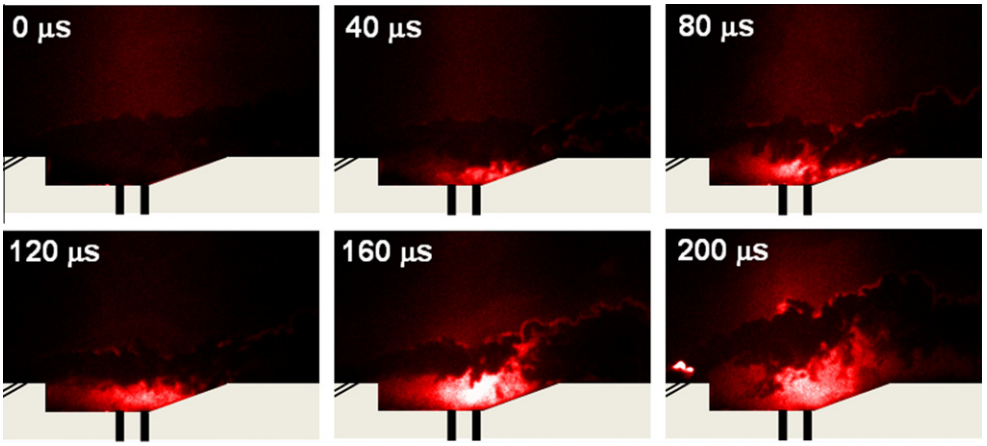

Fig. 6. Time sequential OH PLIF images in the presence of a plasma separated by 40 μs in a run condition 7 flow with a hydrogen jet ($J_n \sim 4.5$).

inside the cavity is clearly ignited at about 40 μs in the presence of the plasma, whereas it is seen to ignite at about 80 μs without the plasma (Fig. 4), indicating that τ_{ign} is shortened by approximately 40 μs due to the plasma. The pulsed plasma serves as a radical source in the cavity producing dissociated and excited species by high energy electron impact. An inspection of the images also reveals that the cavity flame initiates at the plasma region between two electrodes (two black solid lines) at the bottom of the cavity in the 40 μs panel in Fig. 6, which implies that the plasma ignition is faster than the auto-ignition observed on the back wall of the cavity in Fig. 4 at 80 μs. As a result, the cavity flame that is ignited earlier propagates faster and deeper into the freestream flow when compared to the auto-ignited flame.

A marginal case is tested with $h_0 \sim 2.0$ MJ/kg (condition 2) air freestream flow under plasma enhancement (note that auto-ignition is not observed at this flow condition). Fig. 7 shows the OH PLIF image taken at 400 μs after the beginning of the test time (500 μs in run condition 2), and illustrates clearly, that a cavity flame can be ignited by plasma enhancement. While the plasma enhancement leads to ignition, it should be mentioned that the absence of auto-ignition does not necessarily imply that ignition would not take place with greater test time. It is noteworthy that a strong OH intensity region is observed adjacent to the cathode (region within the blue dotted circle in Fig 7). This is further evidence supporting the idea that the plasma initiates ignition of the cavity flame. Most of the radicals produced by the plasma discharge originate from a small region very near the cathode (cathode sheath) because of the high energy electrons accelerated in that region. The high energy electrons are produced by a strong electric field induced by the voltage drop across the cathode sheath, while the voltage drop at the anode is correspondingly smaller in comparison to the cathode voltage drop [23,24]. Consequently, the cavity flame is ignited in the cathode region producing a combustion kernel that then propagates to fill the entire cavity.

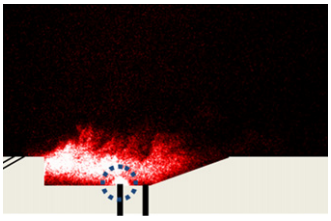

Fig. 7. An OH PLIF image taken with a run condition 2 air flow and a hydrogen jet ($J_n \sim 2.5$).

Similar studies were carried out with ethylene fuel injection to validate the applicability of this plasma-assisted combustion process to a broader range of hydrocarbon fuels of lower flame speed and longer ignition delay time. Fig. 8 shows OH PLIF images taken without the discharge plasma (Fig. 8a) and in the presence of the plasma (Fig. 8c) with ethylene injection ($J_n \sim 3$). The freestream flow corresponds to run condition 7 ($h_0 \sim 2.9$ MJ/kg). The images are taken 200 μs after the beginning of the test time (of approximately 300 μs). The OH PLIF signal observed from within the cavity in the absence of the plasma (Fig. 8a) is comparable to the background noise intensity, whereas a flame is auto-ignited with hydrogen fuel jet injection ($J_n \sim 3.5$) under the same flow condition (Fig. 8b). We attribute this difference to the general findings that the ignition delay times (τ_{ign}) of hydrocarbon fuels (such as ethylene) are longer than those of hydrogen [25]. Therefore, flame holding in a supersonic environment is more difficult to achieve in the case of a hydrocarbon fuel injection compared to the case of hydrogen injection. Fig. 8c depicts a cavity flame of an ethylene fuel jet ignited by the pulsed plasma under the same conditions of Fig. 8a. Filamentary flames in the windward side of the jet as observed with hydrogen injection are not seen in the ethylene jet injection case. However, it is quite apparent that a flame is ignited inside the cavity and the tail of this flame propagates into the freestream flow. It is noteworthy that the extended flame does appear weak and filamentary in structure.

3.3. Effect of jet injection momentum

Jet injection momentum is one of several parameters that affect the propagation of the flame into a freestream flow. Flame propagation into the free stream is crucial to achieving high combustion efficiency and the concomitant release of the maximum amount of energy. Fig. 9 presents a set of Schlieren images depicting varying jet penetration into a freestream flow as a function of normal jet injection to freestream momentum ratio (J_n). The freestream flow corresponds to run condition 2 ($h_0 \sim 2.0$ MJ/kg). The momentum ratio, J_n, of the sonic hydrogen jet is varied from 2 to 10.5 at fixed injection angle of 30°. As shown in the images, jet penetration becomes deeper with increasing J_n. Deeper jet penetration is expected to extend the flame region out of the cavity, only if the discharge plasma enhanced cavity flame provides enough seeding of radicals to ignite a well mixed fuel/oxidizer freestream. The increment of J_n also implies an increase in the fuel mass flow rate in addition to the

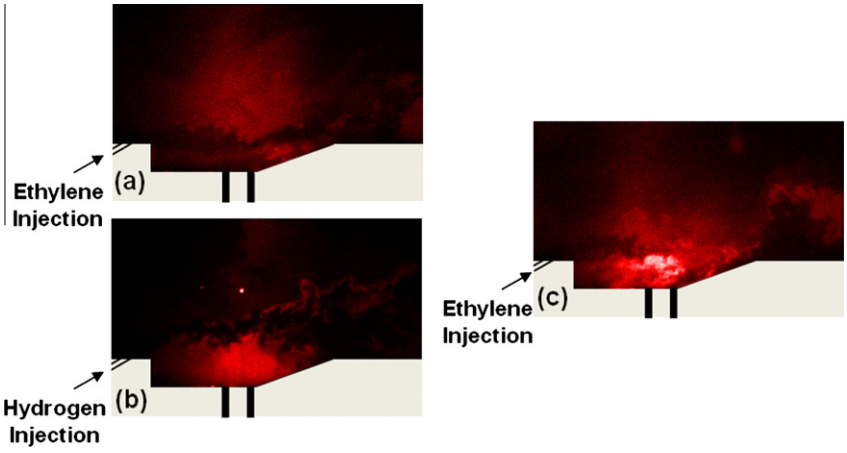

Fig. 8. OH PLIF images taken with a run condition 7 air flow: an ethylene jet injection ($J_n \sim 3$): (a) without a plasma and (c) in the presence of the plasma and (b) hydrogen jet injection ($J_n \sim 3.5$) without the plasma.

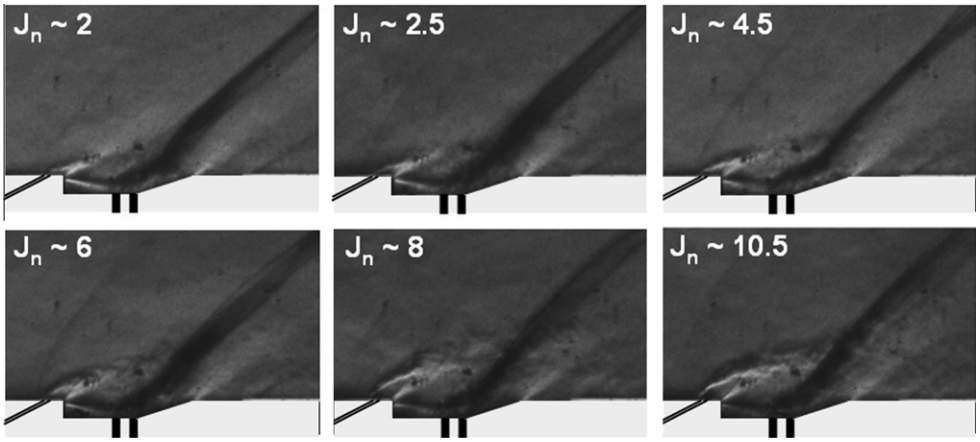

Fig. 9. Schileren images taken with a run condition 2 air flow and hydrogen jet injection of varying J_n.

increased jet penetration, which should also serve to increase the combustion energy release.

OH PLIF images in Fig. 10 depict cavity flames that are ignited by the pulsed discharge plasma under the same flow conditions as in Fig. 9. All of the images are taken 400 μs after the beginning of the test time (approximately 500 μs test time in this case). The OH PLIF images have an adjusted scale to bring out the features, due to the overall weaker signal intensity when compared to the previous high enthalpy cases (e.g. run condition 8 or 7: $h_0 \sim 3.3$ or 2.9 MJ/kg). The intensity scale in Fig. 10 is approximately one seventh of that of Fig. 5. It is apparent from this figure that the lowest value of J_n (~2) produces the strongest flame in the cavity although the flame does not appear to propagate into the freestream flow. It seems as though the flame boundary above the cavity is delineated by the trajectory of the jet core. As J_n is increased, the boundary of the flammable mixture region in the leeward side of the jet (the trajectory of the jet core) extends into the freestream region as shown in Fig. 9. However, cavity flame propagation into the freestream is still not very apparent with the higher J_n. Even more apparent is that the cavity flame becomes weaker with increasing J_n. This trend is attributed to a lower fuel concentration in the cavity with increasing J_n. We find therefore, that the cavity flame's role as a radical source to pilot flame propagation into the free stream diminishes with increasing J_n. A fuel jet injection of high J_n values has merits as previously discussed although it also has a limitation lessening the role of the cavity flame as a radical source for flame propagation. Consequently, these two constraints, opposing each other, demand the choice of a moderate value of J_n, or the use of an alternative method of controlling two important roles played by the fuel jet, namely the seeding of the cavity with fuel to produce, through combustion inside the cavity, a cavity flame that serves as an effective radical source; and the seeding of the freestream to produce a well mixed flow that facilitates the propagation of the cavity flame into the freestream. We have found that the lowest value of J_n that results in significant flame propagation behind the cavity is $J_n \sim 3.5$, as seen in Fig. 5d. On the other hand, relatively strong OH signal (indicative of strong combustion) is observed inside the cavity with J_n lower than 4.5, as seen in Fig. 10, although higher enthalpy conditions or a stronger plasma source would be required to ignite the whole flammable freestream region in this case. In short, an optimized choice of J_n between 3.5 and 4.5 would be preferred with the current cavity configuration.

3.4. Plasma modeling and reaction kinetics simulation

Numerical modeling of the pulsed plasma discharge and reaction kinetics of plasma-assisted combustion process was carried out. The objective was to qualitatively interpret the experimental findings, and to assess the prospects of using higher discharge power to further extend the combustion enhancement.

The diagram in Fig. 11 summarizes the general procedure used in our analysis. The simulation requires the modeling of the pulsed discharge plasma, which is a highly nonequilibrium process, requiring the solution of the Boltzmann equation. We use the commercially-available Boltzmann solver (BOLSIG [26]) to facilitate

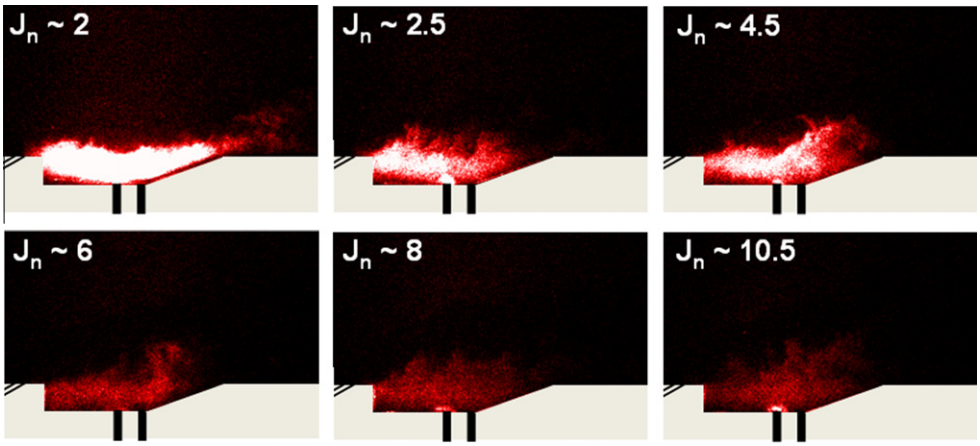

Fig. 10. OH PLIF images taken with a run condition 2 air flow and a hydrogen jet.

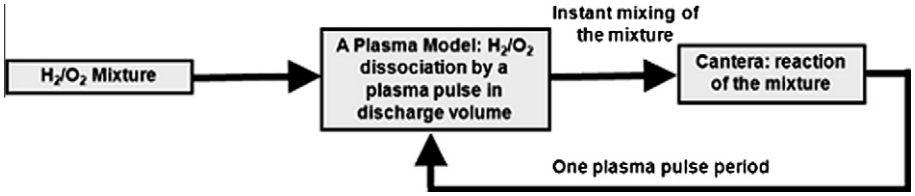

Fig. 11. The schematic of the simulation procedure.

this calculation, given input conditions such as the applied electric field, number density, and species mole fraction. The electron energy distribution derived from the Boltzmann equation provides the rate coefficients of the electron-impact dissociation reactions utilizing dissociation crosssections obtained from the literature [27,28]. The BOLSIG-based calculation accounts only for the presence of the parent molecules (equimolar H_2 and O_2 throughout this simulation study) in the mixture, and does not account for electron collisions with subsequent excited states and dissociation products. The rate coefficients, in accordance with the simplified initial yield calculation method proposed by Penetrante et al. [29,30], allow us to calculate the concentrations of the species dissociated by the pulsed plasma (only direct H_2 and O_2 dissociation reactions by electron impact of H_2 and O_2 (R1) and (R2) are considered in the current study). We consider the following electron-impact dissociation reactions in the simulations:

$$H_2 + e \rightarrow 2H + e \quad (R1)$$

$$O_2 + e \rightarrow 2O + e \quad (R2)$$

The dissociated species are then introduced as initial condition mole fractions into an H_2/O_2 mixture under the flow or static conditions of interest. The simulation of the reaction kinetics of the resulting flammable mixture is facilitated by the use of a MATLAB based code implemented with the Cantera toolbox (http://www.cantera.org; http://azure.caltech.edu/~dgg/cantera/ref/index.html).

The parameters determining the characteristics of the plasma are based on experimental discharge conditions. The reduced electric field (E/N, where, E is the electric field applied between the electrode pair and N is the number density of the neutral molecules in the plasma region) of the pulsed plasma is estimated to be approximately 300 Td. The nominal average power consumed in the plasma region between the electrodes is approximately 10 W, as estimated from the typical experimental discharge voltage and current traces. We note that the electron energy distribution is derived from a quasi-steady state solution of the Boltzmann equation, and also neglects the strong inhomogeneity of the plasma and its composition in the vicinity of the discharge. These simplifications make the modeling tractable, but result in only an approximation

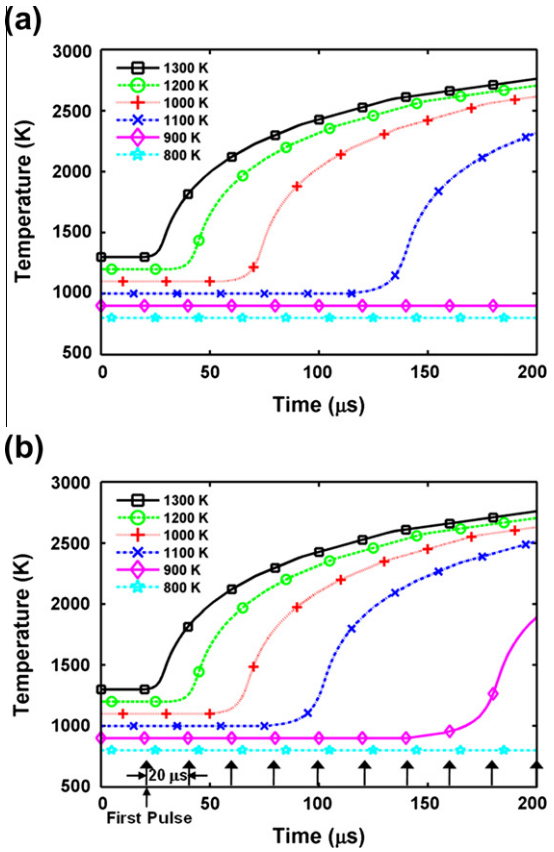

Fig. 12. Temperature of the equimolar H_2/O_2 mixture vs. time: (a) without the pulsed plasma and (b) in the presence of the plasma (50 kHz and 10 W).

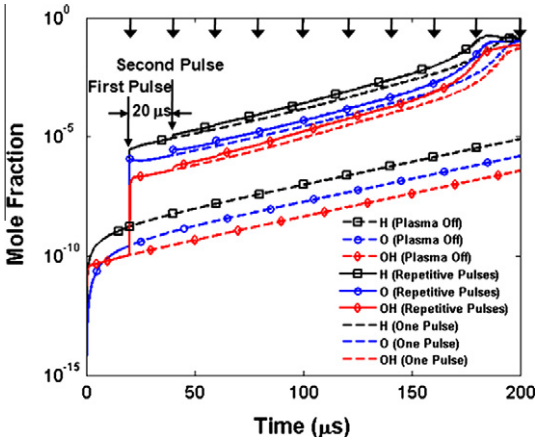

Fig. 13. A graph of the mole fractions of the radicals (H, O and OH) vs. time under 900 K initial temperature condition (equimolar H_2/O_2 mixture).

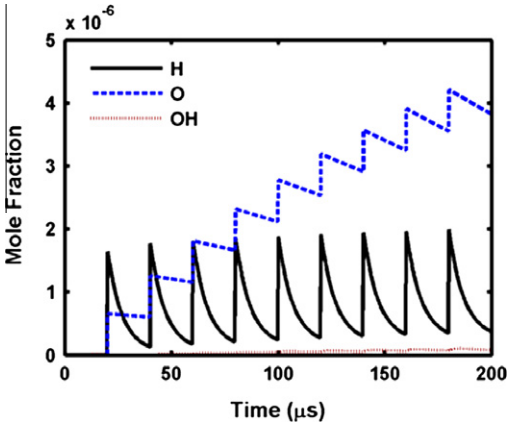

Fig. 14. A graph of the mole fractions of the radicals (H, O and OH) vs. time under 500 K initial temperature condition (equimolar H_2/O_2 mixture).

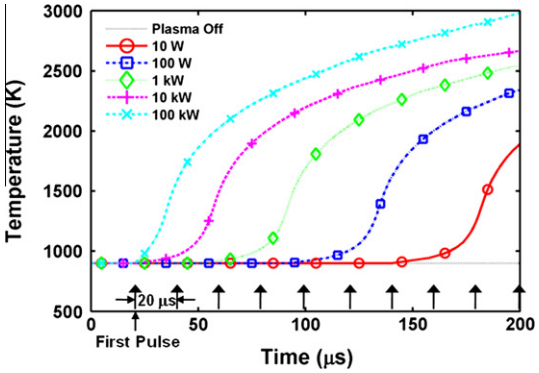

Fig. 15. A graph of the temperature of the equimolar H_2/O_2 mixture vs. time with the pulsed plasma (50 kHz) of varying plasma power from 10 W to 100 kW.

to the more complex physical chemistry that is encountered in this problem. The resulting model is intended to provide a qualitative understanding of the results seen experimentally.

A perfectly stirred reactor (PSR) approach (100 mm^3 nominal volume, determined from an approximately 50 mm^2 cavity area and 2 mm cavity depth) with instant mixing is used to simulate the reaction mechanism driven by the pulsed plasma. The pulsed plasma in the simulation procedure is treated as a simple radical source providing dissociated radical (e.g. O and H) mole fractions periodically into the mixture after initially heating the mixture to some prescribed static temperature. The mixture in the reactor is affected by repeated plasma pulses, as in the cavity experiments, because the relatively static flow conditions within the cavity, as the flow residence time is much longer than the typical pulse period (20 μs with 50 kHz repetition rate). We assume adiabatic conditions in the PSR, as little energy is lost to the walls during the short time periods over which the flame ignites $\ll$1 ms. We also assume that the discharge does not significantly elevate the mixture temperature. The thermal energy is assumed to be dispersed over the reactor volume instantaneously prohibiting a local temperature rise in the discharge region. However, the temperature will increase in time as a result of recombination and/or combustion. The energy supplied by a single discharge pulse is taken to be 0.2 mJ. The simulation spans a time duration of 200 μs while a total of ten plasma pulses, for the case of 50 kHz pulse repetition rate, successively introduces radicals into the equimolar H_2/O_2 mixture. Full details of the simulation can be found in Ref. [31].

3.5. Reduction of ignition delay by the pulsed plasma

Fig. 12 compares the simulated temperature evolution in the PSR without (Fig. 12a) and with (Fig. 12b) the pulsed plasma discharge, for a range of initial static temperature. The first plasma pulse is applied at 20 μs after the initial heating of the mixture, and the temporal locations of the repeated plasma pulses are indicated by the black upward arrows in Fig. 12b. The abrupt temperature rises appearing in the graphs indicate the ignition of the mixture. As shown in Fig. 12a, the ignition delay time shortens with increasing initial mixture temperature. The ignition delay

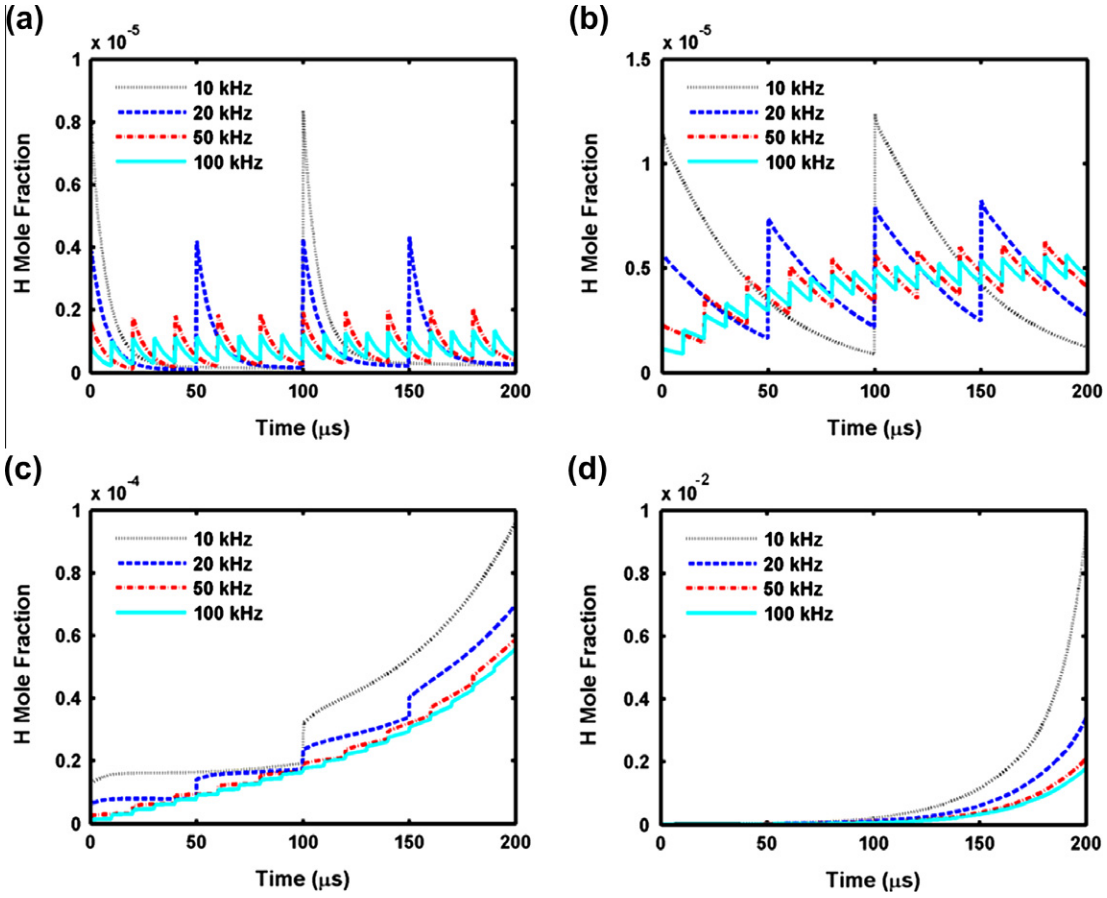

Fig. 16. Graphs of H radical mole fractions vs. time with the pulsed plasma of varying pulse repetition frequency from 10 kHz to 100 kHz under (a): 500 K, (b): 700 K, (c): 800 K, and (d): 850 K initial mixture (equimolar H_2/O_2) temperature conditions.

time is approximately 30 μs at a 1300 K initial static temperature whereas the mixture is not at all ignited within the 200 μs window when the mixture temperature is lower than 900 K. In contrast, shorter ignition delays are observed with the repetitive discharge at any given initial mixture temperature condition, albeit the reduction in ignition delay is increasingly less perceptible as the static temperature is increased, and the plasma is seen to have a negligible effect at temperatures above approximately 1200 K. A 40 μs reduction in ignition delay is seen at a temperature of 1000 K. This delay is comparable to that seen in the experiments, as illustrated in Fig. 4. It is noteworthy that while the conditions of Fig. 4 are for a flow static temperature of 1300 K, we expect the static temperature within the cavity to be much less, due to the entrainment of colder jet fuel.

The predicted evolution in the radical concentrations is shown in Fig. 13. It appears from this calculation, that only the first few discharge pulses are responsible for the ignition of the equimolar mixture (within the 200 μs window) at a static temperature of 900 K. We see that the first discharge pulse causes a significant increase in the radical concentration when compared to that in the absence of the discharge while the effects of the subsequent discharges are increasingly less perceptible. The radical concentrations increase again at a time of about 180 μs concomitant with ignition in the presence of repetitive discharge pulses. As shown in Fig. 13, the ignition with a single discharge pulse applied at 20 μs is also observed at approximately 190 μs, thus confirming the dominant role of the first pulse.

It is noteworthy that the radical supplied by the first discharge pulse at 20 μs amounts to an increase in mole fraction to a level of a mere 10^{-6} indicating that the ignition process is very sensitive to the small amount of injected radicals.

The results of simulations carried out at a lower temperature of 500 K (which is below the minimum temperature for auto-ignition) are shown in Fig. 14. Ignition at these conditions requires multiple plasma pulses. As shown in Fig. 14, there is a successive increase in O radicals whereas the time average H radical concentration is nearly constant. This difference in kinetics is due to the faster consumption of H atoms (e.g. recombination reaction and H_2/O_2 chain/termination reactions) between discharge pulses. Despite the relatively level value in the peak (or average) H atom mole fraction, the plasma still has an indirect benefit on ignition delay, because H recombination is a strongly exothermic reaction, releasing heat to the mixture, further facilitating combustion at times well beyond 200 μs. Like O, the OH mole fractions increase successively, but are at values significantly below those of either H or O.

3.6. Effect of plasma power and pulse repetition frequency

The predicted effect of employing higher discharge power (up to 100 kW of average power) is illustrated in the graph of Fig. 15. For this particular case, the initial mixture static temperature is 900 K and the plasma power is varied (by increasing the pulse energy) from 10 W to 100 kW. As expected, the ignition delay times are reduced with increasing plasma power. Plasma powers higher than 10 kW (200 mJ per pulse) cause an immediate temperature rise coincident with the first plasma pulse. We find that the production of dissociated radicals is, to first-order, proportional to

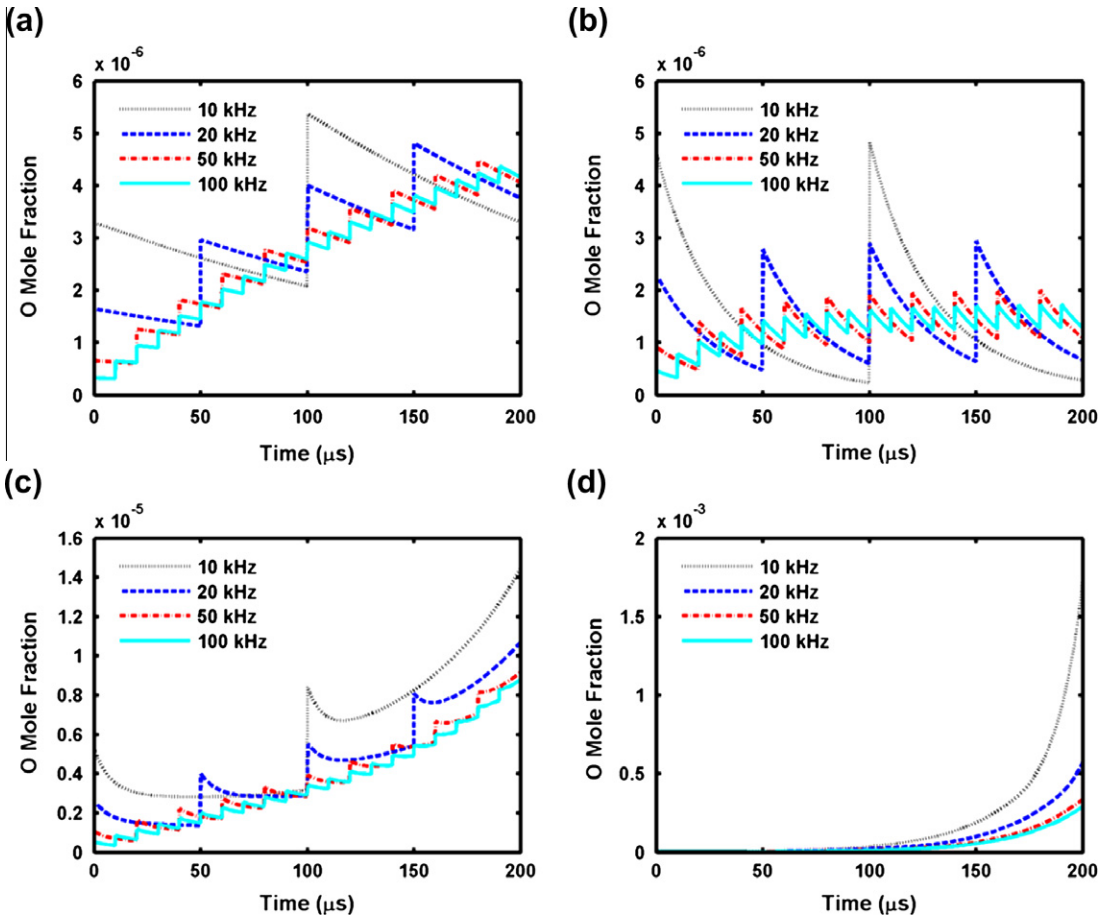

Fig. 17. Graphs of O radical mole fractions vs. time with the pulsed plasma of varying pulse repetition frequency from 10 kHz to 100 kHz under (a): 500 K, (b): 700 K, (c): 800 K, and (d): 850 K initial mixture (equimolar H_2/O_2) temperature conditions.

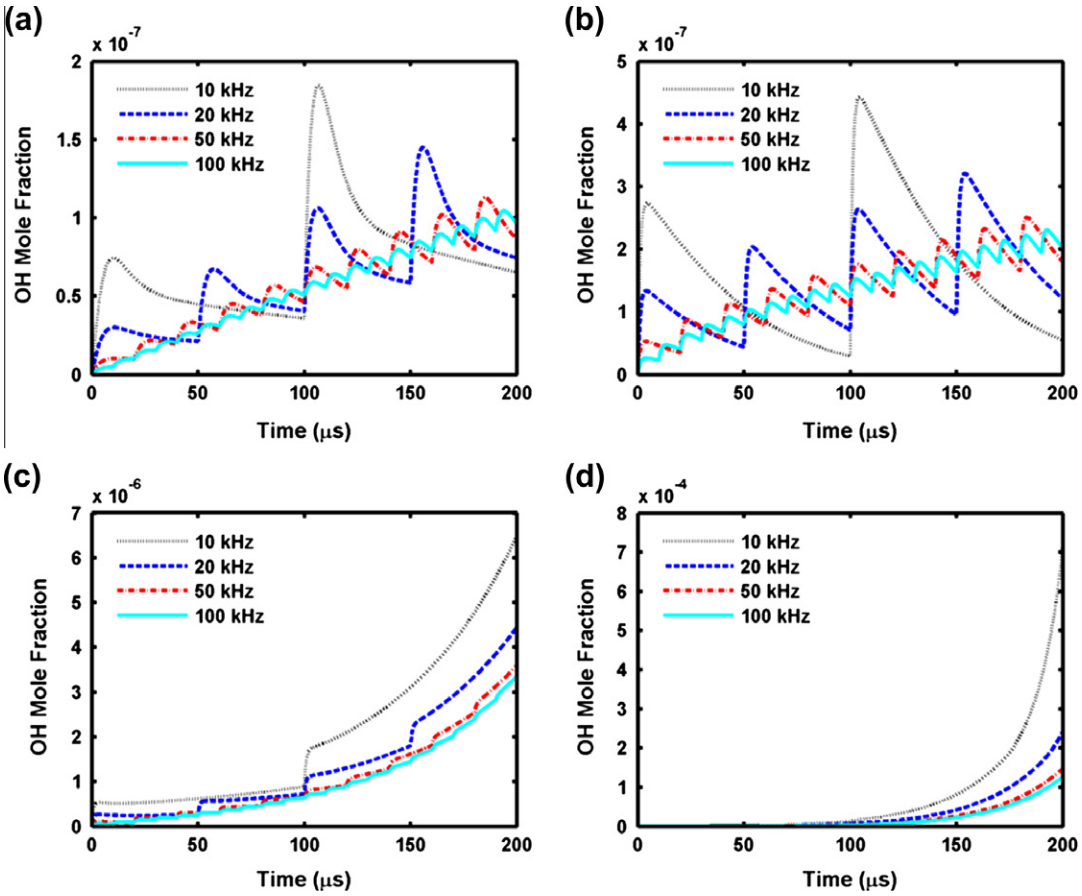

Fig. 18. Graphs of OH radical mole fractions vs. time with the pulsed plasma of varying pulse repetition frequency from 10 kHz to 100 kHz under (a): 500 K, (b): 700 K, (c): 800 K, and (d): 850 K initial mixture (equimolar H_2/O_2) temperature conditions.

the plasma power, and therefore, a thousand-fold increase in plasma power corresponds to a thousand times the radical supply to the mixture in comparison to that of a 10 W plasma. Increasing the average discharge power from 10 W to 10 kW reduces the temperature rise time by a factor of nearly ten, resulting in a much reduced ignition delay.

The effect of pulse discharge frequency at a fixed plasma power (10 W) is illustrated through the model results shown in Figs. 16–18. The graphs of Fig. 16a–d are for H, Fig. 17a–d are for O, and Fig. 18a–d are for OH radicals. The pulse discharge frequency is varied from 10 kHz to 100 kHz under (a): 500 K, (b): 700 K, (c): 800 K and (d): 850 K initial static temperature conditions of the equimolar H_2/O_2 mixture. For comparison of the radical production in the simulation time span (200 μs), the first pulse of all cases is applied at the time of $t = 0$ μs. An increase in pulse frequency at constant average discharge power is seen (as expected) to reduce the level of radical production because of the reduction in pulse energy. We also see that lower frequencies allow for increased recombination between pulses, particularly at lower static temperatures. At higher static temperature, e.g., 800 K in Figs. 16c, 17c and 18c, and 850 K in Figs. 16d, 17d and 18d, runaway radical production occurs, even at the lower pulse frequencies, as combustion is initiated shortly after the first pulse. It is noteworthy that the OH mole fractions are slightly out of phase with the H and O mole fractions – a consequence of the fact that OH is itself not produced directly by electron-impact dissociation (in our simulations), and is instead produced by chain/recombination reactions and H/O reactions with product species such as HO_2 and H_2O_2 (R3)–(R11):

$$H + O_2 \rightarrow O + OH \quad (R3)$$
$$O + H_2 \rightarrow H + OH \quad (R4)$$
$$O + H_2O \rightarrow OH + OH \quad (R5)$$
$$O + H + M \rightarrow OH + M \quad (R6)$$
$$HO_2 + H \rightarrow OH + OH \quad (R7)$$
$$HO_2 + O \rightarrow OH + O_2 \quad (R8)$$
$$H_2O_2 + M \rightarrow OH + OH \quad (R9)$$
$$H_2O_2 + H \rightarrow H_2O + OH \quad (R10)$$
$$H_2O_2 + O \rightarrow OH + HO_2 \quad (R11)$$

These reactions [32] are prompted by the sudden increase of H/O radicals supplied by the plasma. Therefore, the peaks in OH mole fractions appear to be slightly delayed in time relative to the discharge pulses.

For the results shown in Figs. 16–18, the total energy deposited over the 200 μs time span is the same for all discharge frequency cases. However, the radical mole fractions arrived at towards the end of the time computed are noticeably different. This difference in resulting properties depends on initial mixture temperature because the first plasma pulse (say at 10 W), regardless of the pulse frequency, can ignite the mixture under high temperature conditions (>800 K) as seen in the conditions depicted in Fig. 13. In that case, only the radical production by the first plasma pulse, which is dependent on pulse energy (not average power), is responsible for the ignition. An additional sensitivity to initial temperature is a result of the fact that radical consumption and production rates also depend strongly on temperature. In Figs. 16–18a and b, the recombination reaction times are nominally comparable to the time be-

tween the discharge pulses (rapid radical decay within 20 μs pulse period), and as a result, there is much benefit to using higher pulse repetition frequencies – plasma provides more radicals as a result of the same energy deposition (2 mJ in 200 μs). For example, the H mole fractions at 200 μs are 5.52×10^{-7} (Fig. 16a) and 4.75×10^{-6} (Fig. 16b) with 100 kHz frequency, while they are only 2.30×10^{-7} (Fig. 16a) and 1.23×10^{-6} (Fig. 16b) with 10 kHz frequency. In contrast, the radical production at lower pulse frequency is greater in Figs. 16–18c under the higher initial mixture temperature condition (800 K). In this case, radical production is faster than radical recombination, and the radical concentration increases between the plasma pulses. In Figs. 16–18d, the mixture is ignited earlier with the lower discharge pulse frequency because of the greater pulse energy. The H mole fractions at 200 μs are 5.57×10^{-5} (Fig. 16c) and 1.79×10^{-4} (Fig. 16d) with 100 kHz frequency, while they are 9.62×10^{-5} (Fig. 16d) and 9.42×10^{-4} (Fig. 16d) with 10 kHz frequency.

4. Conclusions

We have presented an experimental study of cavity flame stabilization assisted by a nonequilibrium pulsed discharge plasma in supersonic flows. The supersonic air flow is generated in an expansion tube, producing a test time of approximately 300–500 μs in which an oblique hydrogen jet is injected into the flow upstream of a cavity flame-holder. The use of the cavity results in flame ignition in the leeward side of the oblique hydrogen jet. The cavity flame is auto-ignited when the enthalpy of the free-stream is higher than 2 MJ/kg. In conjunction with the use of the cavity, a nanosecond pulsed discharge is applied inside the cavity to enhance flame ignition. A noticeable reduction in the ignition delay of the mixture within the cavity is seen for a range of flow conditions. This enhancement is also seen for ethylene jet injection, suggesting that this plasma-assisted combustion process is extendable to other hydrocarbons.

The scope of the experimental studies was limited in part by the maximum discharge power available for our nanosecond pulse discharge source (~10 W average power at 50 kHz pulse rate). Simple model calculations were therefore carried out, to qualitatively validate our experimental results and to investigate the potential extrapolation of the use of nonequilibrium pulsed plasmas for ignition and flame holding at conditions not achievable in our present operating configuration. With the pulsed plasma modeled as a radical source dissociating H_2 and O_2 to produce H and O by electron impact, it was found that the plasma (at the relatively low power conditions of 10 W and 50 kHz) is capable of significantly reducing the ignition delay time of the H_2/O_2 mixture by amounts that are in agreement with experimental findings. A parametric study indicated that higher average powers (higher pulse energy) can further reduce the ignition delay. Ignition is predicted to occur almost immediately following a single 200 mJ pulse discharge pulse in 900 K equimolar H_2/O_2 mixtures. Simulations were also carried out for varying discharge pulse repetition rates (up to 100 kHz) at a fixed power (10 W). The sensitivity of flame ignition and flame holding to pulse repetition rate depends strongly on the initial temperature of the H_2/O_2 mixture. For a fixed average discharge power, a higher repetition rate produces more H and O in a 200 μs time span under low temperature conditions (500–800 K), while a lower rate (having a higher pulse energy) is found to ignite higher temperature mixtures (900 K) in shorter times.

Acknowledgments

This work is sponsored by the AFOSR/MURI Program–Experimental/Computational Studies of Combined-Cycle Propulsion: Physics and Transient Phenomena in Inlets and Scramjet Combustors with Julian Tishkoff as the Technical Monitor.

References

[1] A. Ben-Yakar, R.K. Hanson, J. Propul. Power 17 (2001) 869–877.
[2] C.C. Rasmussen, J.F. Driscoll, C.D. Carter, K.Y. Hsu, J. Propul. Power 21 (2005) 765–768.
[3] M.R. Gruber, J.M. Donbar, C.D. Carter, K.Y. Hsu, J. Propul. Power 20 (2004) 769–778.
[4] L. Maddalena, T.L. Campioli, J.A. Schetz, AIAA-2005-3235, in: AIAA/CIRA 13rd Int. Space Planes and Hypersonics Systems and Tech. Conf., Capua, Italy, 2005.
[5] C.D. Anderson, J.A. Schetz, J. Propul. Power 21 (2005) 371–374.
[6] S.B. Leonov, D.A. Yarantsev, A.P. Napartovich, I.V. Kochetov, IEEE Trans. Plasma Sci. 34 (2006) 2514–2525.
[7] R.C. Rogers, D.P. Capriotti, R.W. Guy, AIAA-98-2506, in: 20th AIAA Advanced Measurement and Ground Testing Tech. Conf., Albuquerque, NM, 1998.
[8] K.M. Kim, S.W. Baek, C.Y. Han, Int. J. Heat Mass Transfer 47 (2004) 271–286.
[9] K. Lin, C. Tam, I. Boxx, C. Carter, K. Jackson, M. Lindsey, in: 43rd AIAA/ASME/SAE/ASEE Joint Propulsion Conference and Exhibit, Cincinnati, OH, 2007.
[10] T. Fang, M. Ding, J. Zhou, Front. Energy Power Eng. China 2 (4) (2008) 528–533.
[11] C.D. Cathey, T. Tang, T. Shiraishi, T. Urushihara, A. Kuthi, M.A. Gundersen, IEEE Trans. Plasma Sci. 35 (2007) 1664–1668.
[12] S.A. Bozhenkov, S.M. Starikovskaia, A.Yu. Starikovskii, Combust. Flame 133 (2003) 133–146.
[13] V.P. Zhukov, A.E. Rakitin, A.Yu. Starikovskii, AIAA 2007-1029, in: 45th AIAA Aerospace Sciences Meeting and Exhibit, Reno, NV, 2007.
[14] G.L. Pilla, D.A. Lacoste, D. Veynante, C.O. Laux, IEEE Trans. Plasma Sci. 36 (2008) 940–941.
[15] I.V. Adamovich, I. Choi, N. Jiang, J.-H. Kim, S. Keshav, W.R. Lempert, E. Mintusov, M. Nishihara, M. Samimy, M. Uddi, Plasma Sources Sci. Technol. 18 (2009) 034018.
[16] I.I. Esakov, L.P. Grachev, K.V. Khodataev, V.A. Vinogradov, D.M. Van Wie, IEEE Trans. Plasma Sci. 34 (2006) 2497–2506.
[17] W.N. Heltsley, J.A. Snyder, A.J. Houle, D.F. Davidson, M.G. Mungal, R.K. Hanson, AIAA 2006-4443, in: 42nd AIAA/ASME/SAE/ASEE Joint Propulsion Conf. and Exhibit, Sacramento, CA, 2006.
[18] G.S. Settles, Schlieren and Shadowgraph Techniques, Springer-Verlag, New York, 2006.
[19] W.N. Heltsley, J.A. Snyder, C.C. Cheung, M.G. Mungal, R.K. Hanson, AIAA 2007-5401, in: 43rd AIAA/ASME/SAE/ASEE Joint Propulsion Conf. and Exhibit, Cincinnati, OH, 2007.
[20] J.L. Alcock, L.C. Shirvill, R.F. Cracknell, Technical Report of the European Community, ENK6-CT2000-00442, 2001.
[21] J.E. Fay, T. Rossmann, AIAA 2006-1230, in: 44th AIAA Aerospace Sci. Meeting and Exhibit, Reno, NV, 2006.
[22] S. Kawai, S.K. Lele, in: Center for Turbulence Research Annual Research Briefs, 2007, pp. 353–365.
[23] Z. Wronski, Vacuum 78 (2005) 641–647.
[24] J.L.T. Fabela, J.O. Pacheco-Sotelo, M.P. Pacheco, J.S. Benítez-Read, R. López-Callejas, G. Zissis, S. Bhosle, IEEE Trans. Plasma Sci. 35 (2007) 1104–1110.
[25] P. Gokulakrishnan, S. Pal, M.S. Klassen, A.J. Hamer, R.J. Roby, O. Kozaka, S. Menon, AIAA 2006-5092, in: 42nd AIAA/ASME/SAE/ASEE Joint Propulsion Conference and Exhibit, Sacramento, CA, 2006.
[26] http://www.siglo-kinema.com/bolsig.htm.
[27] S.J.B. Corrigan, J. Chem. Phys. 43 (1965) 4381–4386.
[28] D.A. Vroom, F.J. de Heer, J. Chem. Phys. 50 (1969) 580–590.
[29] B.M. Penetrante, M.C. Hsiao, B.T. Merritt, G.E. Vogtlin, P.H. Wallman, M. Neiger, O. Wolf, T. Hammer, S. Broer, Appl. Phys. Lett. 68 (1996) 3719–3721.
[30] W. Kim, M.G. Mungal, M.A. Cappelli, Appl. Phys. Lett. 92 (2008) 051503.
[31] H. Do, Ph.D. Dissertation, Mechanical Engineering Department, Stanford University, Stanford, CA, 2009.
[32] J. Li, Z. Zhao, A. Kazakov, F.L. Dryer, Int. J. Chem. Kinet. 36 (2004) 566–575.